Benzyl alcohol-treated CH3NH3PbBr3 nanocrystals exhibiting high luminescence, stability, and ultralow amplified spontaneous emission thresholds

Veldhuis, Sjoerd Antonius; Tay, Eugene Yong Kang; Bruno, Annalisa; Dintakurti, Sai S. H.; Bhaumik, Saikat; Muduli, Subas Kumar; Li, Mingjie; Mathews, Nripan; Sum, Tze Chien; Mhaisalkar, Subodh Gautam

2017

Veldhuis, S. A., Tay, E. Y. K., Bruno, A., Dintakurti, S. S. H., Bhaumik, S., Muduli, S. K., . . . Mhaisalkar, S. G. (2017). Benzyl alcohol-treated CH3NH3PbBr3 nanocrystals exhibiting high luminescence, stability, and ultralow amplified spontaneous emission thresholds. Nano Letters, 17(12), 7424-7432. doi:10.1021/acs.nanolett.7b03272

https://hdl.handle.net/10356/141120

https://doi.org/10.1021/acs.nanolett.7b03272

Benzyl Alcohol-treated $CH_3NH_3PbBr_3$ Nanocrystals Exhibiting High Luminescence, Stability and Ultralow Amplified Spontaneous Emission Thresholds

Sjoerd A. Veldhuis,[1,‡] Yong Kang Eugene Tay,[2,‡] Annalisa Bruno,[1,2] Sai S.H. Dintakurti,[1] Saikat Bhaumik,[1] Subas Kumar Muduli,[1] Mingjie Li,[2] Nripan Mathews,[1,3] Tze Chien Sum[2], and Subodh G. Mhaisalkar[1,3]**

[1]Energy Research Institute at NTU (ERI@N), Research Techno Plaza, X-Frontier Block Level 5, 50 Nanyang Drive, Singapore 637553, Singapore.

[2]Division of Physics and Applied Physics, School of Physical and Mathematical Sciences, Nanyang Technological University, 21 Nanyang Link, Singapore 637371, Singapore.

[3]School of Materials Science and Engineering, Nanyang Technological University, 50 Nanyang Avenue, Singapore 639798.

KEYWORDS. Perovskites, quantum dots, ligand coordination, light emission, lasing, optoelectronics.

ABSTRACT. We report the high yield synthesis of ca. 11 nm-sized $CH_3NH_3PbBr_3$ nanocrystals with near-unity photoluminescence quantum yield. The nanocrystals are formed in presence of surface-binding ligands through their direct precipitation in a benzyl alcohol/toluene phase. The benzyl alcohol plays a pivotal role in steering the surface ligands binding motifs on the NC surface, resulting in enhanced surface-trap passivation and near-unity PLQY values. We further demonstrate that thin films from purified $CH_3NH_3PbBr_3$ nanocrystals are stable >4 months in air, exhibit high optical gain (ca. 520 cm^{-1}) and display stable, ultra-low amplified spontaneous emission thresholds 13.9 ± 1.3 and 569.7 ± 6 μJ cm^{-2} at one-photon (400 nm) and two-photon (800 nm) absorption, respectively. To the best of our knowledge, the latter signifies a 5-fold reduction of the lowest reported threshold value for halide perovskite nanocrystals to date, which makes them ideal candidates for light-emitting and low-threshold lasing applications.

Solution-processed organic-inorganic halide perovskites of general formula ABX_3 (A = $CH_3NH_3^+$, $HC(NH_2)_2^+$ or Cs^+; X = Cl^-, Br^-, or I^-) have transformed the field of photovoltaics. Owing to their facile phase formation, abundant/inexpensive precursors, and extraordinary optoelectronic properties (e.g. large charge carrier diffusion lengths, balanced electron-hole mobility, direct bandgap, etc.), record power conversion efficiencies surpassing 22% were achieved.[1, 2] More recent achievements include also the demonstration of bright light-emitting diodes (LEDs),[3-9] lasers,[10-13] and photodetectors.[14] Perovskite nanocrystals (NCs), in particular, are promising candidates as gain medium due to their high photoluminescence quantum yield (PLQY), narrow emission width, and full spectral range tunability by virtue of halide substitution or exchange.[15-17] For example, low amplified spontaneous emission (ASE) thresholds across the full visible spectrum were demonstrated for 10 nm-sized all-inorganic $CsPbX_3$ (X = Cl^-, Br^-, or I^-) NCs;[18-20] superior to traditional metal chalcogenide semiconductor quantum dots (QDs). Notably, other halide perovskites such as $CH_3NH_3PbBr_3$ NCs and nanowires,[21, 22] $HC(NH_2)_2PbX_3$ (X = Br^- and I^-) NCs,[23, 24] $CsSnI_3$,[25] and and $HC(NH_2)_2SnI_3$ thin films[26] also displayed low ASE thresholds. These low thresholds may be attributed to the large absorption coefficients of the halide perovskites, the low bimolecular recombination and slow Auger recombination processes. In addition, Pan *et al.* demonstrated that surface-passivated $CsPbBr_3$ NC films also display two-photon absorption processes,[18] which may further expand the use of these perovskite materials in nonlinear optical applications, such as multiphoton excited PL/ASE lasing.

The organic-inorganic halide perovskite NCs are commonly prepared by ligand-assisted re-precipitation (LARP) methods at temperatures <60 °C. Typically, the dissolved molecular precursors are injected into a non-coordinating solvent in the presence of coordinating ligands, aiding the NCs formation and stabilization. Besides luminescent $CH_3NH_3PbBr_3$ NCs,[9, 22, 27-30]

nanoplatelets (NPLs)[31-34] and core-shell NCs[35] were also successfully synthesized. Through careful optimization of the reaction parameters such as choice/amount of ligands and solvents, the PLQY of the resultant NCs rapidly increased from approximately 20% to near-unity values.[27, 29] Notably, the presence of ligands helps to inhibit the crystal growth, while passivating the surface defects and enhancing the colloidal stability.

Despite their impressive optoelectronic properties, the inherent moisture instability of halide perovskites remains problematic during fabrication, storage, and device operation. Efforts to improve the structural stability include, for example, the use of multiple A-site cations (intrinsic),[36] core-shell formation,[35] embedding in polymer matrix,[37] or surface passivation with silanes,[38-40] or cucurbit[7]uril and 2-adamantylammonium ligands (extrinsic).[29] Similarly, didodecyl dimethylammonium bromide (DDAB) has been used to passivate the surface of $CsPbBr_3$ NCs, resulting in improved stability under ambient conditions, as well as under continuous illumination for 34 h at high fluence.[18] Here, concomitantly to the improved photostability, the effective surface passivation resulted in near-unity PLQY. In this work, aliphatic amines and fatty acids were employed as ligands during the nanocrystal synthesis, in combination with benzyl alcohol. The latter has been extensively used in the synthesis of a large variety of (perovskite) metal oxide nanostructures,[41] and is known to play an active role as ligand itself; able to bind to metal atoms and inhibit nanocrystal growth.[42]

Herein, we report the high-yield synthesis of luminescent $CH_3NH_3PbBr_3$ NCs through direct precipitation of the chemical precursors in a benzyl alcohol/toluene phase. The benzyl alcohol (BnOH) plays a pivotal role in steering the passivating ligands and controlling the ligand binding motifs on the NC surface, resulting in significantly improved optoelectronic properties and structural stability. Likewise, it also helped increase the overall reaction yield (ca. 95%) through

rapid precipitation of the NCs during synthesis. The obtained nanocrystals showed narrow PL emission (FWHM ~19 nm) at ca. 525 nm with near-unity PLQY (95-99%). Nanocrystal thin films exhibited high optical gain, ultra-low ASE thresholds, and outstanding photostability, which remained virtually unchanged after 4 months storage under ambient conditions (50% RH).

The highly luminescent $CH_3NH_3PbBr_3$ NCs were prepared via a modified ligand-assisted reprecipitation protocol (**see Figures S1 and S2**), in which the dissolved methylammonium bromide and lead bromide precursors were swiftly injected in absence of coordinating ligands into a 'poor' solvent containing the ligands and BnOH (see **Supporting Information for Materials and Methods**). A bright yellowish-green solution was instantly formed after precursor injection, whereas the control experiment, carried out in absence of BnOH, showed much slower reaction kinetics (i.e. the reaction mixture was visually identical after approximately 30 s). Analogous to slightly polar solvents commonly employed during post-synthetic NC purification (e.g. *n*- and *t*-butanol), the BnOH aids the precipitation of the formed NCs to increase the reaction yield, albeit in our case during nanocrystal formation. The NCs were then purified through centrifugation and removal of the supernatant phase (S1). Subsequently, the precipitated NCs (P1) were redispersed in 2 mL fresh toluene and 2 µL *n*-octylamine (OctAm) was added to the mixture and centrifuged again. The second supernatant phase (S2) was discarded, and the NC precipitate (P2) redispersed in toluene and used for further experiments. **Figure 1a** shows the typical PL emission and absorption characteristics during NC purification. Following the first centrifugation, a clear S1 phase, containing only a small fraction of blue-emitting NPLs (PL emission at ca. 432 nm), was obtained; thus indicating that all NCs were successfully precipitated (**see Figure S3**). The control samples, on the other hand, yielded a bright green supernatant phase (S1c) containing blue-

emitting NPLs and a variety of very small (i.e. quantum-confined) $CH_3NH_3PbBr_3$ NCs, as observed by the multiple PL maxima at 450, 470, and 505 nm (see Figure S3b).

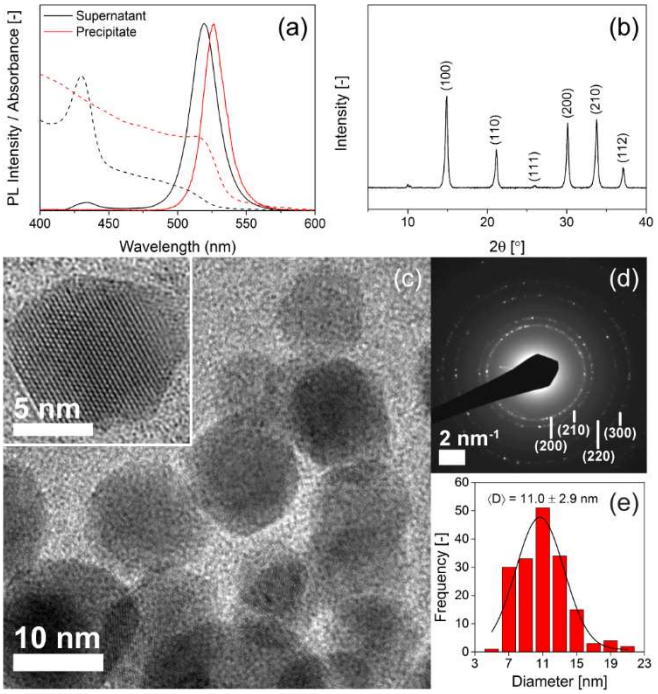

Figure 1. Structural characterization of purified $CH_3NH_3PbBr_3$ NCs prepared with benzyl alcohol. **(a)** Photoluminescence (solid line) and absorbance (dashed line) spectra of the supernatant (S2; red) and precipitate (P2; black) phases, respectively. **(b)** X-ray diffraction pattern. **(c)** HRTEM image of ensemble on $CH_3NH_3PbBr_3$ NCs (P2). Inset: single NC at higher magnification, showing the highly crystalline nature of the NCs. **(d)** Selected-area electron diffraction (SAED) pattern obtained from a large ensemble of NCs. The obtained lattice spacings corroborate with the XRD pattern in (b). **(e)** Crystallite size distribution obtained from HRTEM at low magnification from >150 NCs.

After NC purification, both control and BnOH-containing NCs (P2c and P2, respectively) showed PL maxima at approximately 525-526 nm, and optical bandgaps of 2.33 eV. The addition of OctAm may also facilitate the formation of nanoplatelets (NPLs) during purification, as witnessed in S2 from the excitonic absorption peak at ca. 425 nm and small PL emission at similar wavelength (Figure 1a). These NPLs are absent in the final precipitate. To prevent these NPLs from forming, branched ligands, e.g. triethylamine (TEAm), may be employed during purification. Due to the branching, 2D layered perovskites are inhibited to form, and only band edge absorption and PL emission of the $CH_3NH_3PbBr_3$ were observed (**Figure S4**).

Structural investigation by means of X-ray diffraction (Figure 1b) showed that the NCs were phase-pure and of cubic perovskite structure (lattice constant 5.937(2) Å, $Pm\bar{3}m$ space group), which corroborates well with our recorded selective-area electron diffraction (SAED) patterns (Figure 1d) and reported literature values.[43] Further analysis of the peak broadening in the diffraction patterns with the Scherrer equation, yielded an average crystallite size of ~11 nm, which was supported by detailed HR-TEM analysis of the NCs (Figure 1c,e). The NCs prepared in absence of BnOH, showed identical crystal structure (in both XRD and SAED) and morphology, albeit the average crystallite size of ~10 nm was slightly smaller (**see Figure S5**). X-ray photoelectron spectroscopy (XPS) analysis further showed that both samples exhibited a small bromide deficiency, with Pb:Br is 1:2.78 and 1:2.72 for BnOH-prepared and control samples, respectively. Interestingly, however, the NCs synthesized with BnOH displayed significantly improved structural stability compared to the control samples. Thermogravimetric analysis (TGA) conducted on both samples showed the thermal degradation of NCs prepared with BnOH occurred at 300 °C, approximately 70 °C higher than observed for the samples prepared in absence of BnOH (**see Figure S6**).

Detailed ultrafast spectroscopic studies on thin films of our $CH_3NH_3PbBr_3$ NCs prepared with BnOH revealed ultralow amplified spontaneous emission (ASE) thresholds, high stability under ambient storage/measurement conditions, as well as outstanding optical gain signatures, rendering them as suitable medium in strong coherent light-emitting applications. (**Figure 2**). Nanocrystal thin films were obtained after dropcasting the NCs in toluene on a cleaned Quartz substrate (inset Figure 2a). Using steady-state PL, we ascertained that the carriers responsible for the observed PL emission at 530 nm with a FHWM of ~22 nm (Figure 2a), originate from excitonic emission (see **Figure S7**). Upon increased pump fluence, the one-photon absorption (1PA) signature manifested itself, and eventually dominated, as a red-shifted peak around 548 nm with a concurrent narrowing of the peak width (FWMH ~6.5 nm). From the integrated light intensity, an average ASE threshold at approximately F_{th} ~14 μJ cm^{-2} was determined for our dropcasted NC thin films; similar to the lowest recorded thresholds for organic-inorganic and all-inorganic perovskite NCs,[19, 20, 23, 44] and colloidal semiconductor quantum dots (QDs) in general.[45-48] Analogously, the non-linear two-photon pumped absorption (2PA) process yielded ASE thresholds of F_{th} ~570 μJ cm^{-2} (Figure 2c,d). To the best of our knowledge, this represents the lowest non-linear absorption threshold recorded for halide perovskites; approximately 5-20x lower than reported thus far (see **Table 1**).[18, 49, 50] The one- and two-photon cross-sections were also determined using the Z-scan technique[51] (**see Figure S8**), to further corroborate the outstanding low ASE thresholds. Here, dilute colloidal NC solutions (conc. $1.48 \cdot 10^{-5}$ mol dm^{-3}) were used in order to avoid re-absorption and scattering effects. The 1PA and 2PA cross-sections were $\sigma_{abs}^{(1)} = (1.4 \pm 0.4) \cdot 10^{-13}$ cm^2 and $\sigma_{abs}^{(2)} = (1.0 \pm 0.2) \cdot 10^5$ GM (where 1 GM = 10^{-50} cm^4 s), respectively, which compares favorably to other halide perovskite and CdSe/ZnS chalcogenide nanocrystal systems.[19, 20, 52]

Table 1. Overview of selected representative results of one-photon (1PA) and two-photon (2PA) amplified spontaneous emission thresholds (F_{th}) from organic-inorganic and all-inorganic halide perovskite gain media.

First Author [journal, year]	Material [morphology]	Emission Color	1PA F_{th} [μJ cm^{-2}]	2PA F_{th} [μJ cm^{-2}]	Ref.
Veldhuis et al. [This Work]	**$CH_3NH_3PbBr_3$ [NCs]**	**Green**	**13.9**	**569.7**	**-**
Priante et al. [APL, 2015]	$CH_3NH_3PbBr_3$ [NCs]	Green	350[c)]	n.r	21
Vybornyi et al. [Nanoscale, 2016]	$CH_3NH_3PbBr_3$ [NWs][a)]	Green	3.0	n.r	22
Yang et al. [ACS Appl. Mater. Int., 2016]	$CH_3NH_3PbBr_3$ [μDisk]	Green	n.r.	2,200	50
Yakunin et al. [Nat. Commun., 2015]	$CsPbBr_3$ [NCs]	Green	5	n.r.	20
Wang et al. [Adv. Mater., 2015]	$CsPbBr_3$ [NCs]	Green	22	n.r.	19
Wang et al. [Nano Lett., 2016]	$CsPbBr_3$ [NCs]	Green	n.r.	2,500[d)]	49
Pan et al. [JPCL, 2015]	$CsPbBr_3$ [NCs]	Green	192	12,000	18
Tong et al. [Angew. Chem. Int. Ed., 2016]	$CsPbBr_3$ [NCs]	Green	2.1	n.r.	44
Protesescu et al. [JACS, 2016]	$HC(NH_2)_2PbBr_3$ [NCs]	Green	14	n.r.	23
Protesescu et al. [ACS Nano, 2017]	$Cs_{1-x}[HC(NH_2)_2]_xPbI_3$ [NCs][b)]	Red-NIR	7.5-28	n.r.	24

[a)] Nanowires; [b)] $HC(NH_2)_2PbI_3$ (x = 1) and $Cs_{0.9}[HC(NH_2)_2]_{0.1}PbI_3$ (x = 0.1), respectively; [c)] Measured at λ_{ex} = 475 nm; [d)] 3PA 5.2 mJ cm^{-2}.

In addition, the NC films displayed superb structural and photochemical stability after 4 months of storage under ambient conditions (22 °C, 50% RH), as both the PL and ASE emission peak positions and ASE thresholds remain virtually unchanged (Figure 2e,f). Despite similar ASE thresholds under one-photon pumped excitation (ca. 16 μJ cm^{-2}), control samples prepared in

absence of BnOH, show significantly higher thresholds two-photon excitation at approx. 850 μJ cm^{-2} (see Figure 2f). Also, their structural and photochemical stability were in stark contrast to the samples prepared with BnOH. After 4 months storage in air, the control samples' 1PA ASE threshold nearly tripled to F_{th} = 48 μJ cm^{-2}, and the 2PA threshold increased ca. 1.5x to approx. F_{th} ~1.17 mJ cm^{-2}. This indicates that the benzyl alcohol assists in successfully passivating the NC surface, thereby increasing the robustness towards chemical or photochemical changes of the $CH_3NH_3PbBr_3$ NCs under ambient conditions. The photo-chemical stability parameters are collated for ease of comparison in **Table 2**.

Table 2. Overview of 1PA and 2PA characteristics of dropcasted thin films after storage of 4 months under ambient conditions. All films are prepared from $CH_3NH_3PbBr_3$ NCs synthesized with BnOH.

	1PA (400 nm excitation)			2PA (800 nm excitation)		
	Fresh	2 months	4 months	Fresh	2 months	4 months
λ_{PL} [nm][a)]	530.2	530.1	530.2	528.3	530.1	531.1
λ_{ASE} [nm]	546.1	546.9	546.2	545.3	546.1	546.2
E^B_{xx} [meV][b)]	68.1	71.8	68.5	73.2	68.5	66.5
F_{th} [μJ cm^{-2}][c)]	14±1.3	15.1±0.3	12.5±0.3	542±6	589±6	578±6
$\Delta\lambda_{PL}$ [nm][d)]	23.5	23.0	22.2	23.0	23.3	20.0
$\Delta\lambda_{ASE}$ [nm]	6.8	5.5	5.6	6.0	7.0	6.0

[a)] PL and ASE emission wavelength; [b)] Exciton binding energy; [c)] ASE threshold; [d)] FWHM of PL and ASE emission (i.e., at low and high pump fluence, respectively).

We attribute the physical origin of the light amplification in the ASE spectra due to the formation (and subsequent emission) of biexciton (XX) radiative recombination. Generally, under high fluence pumping conditions, the average amount of generated excitons within each nanocrystal $\langle N \rangle$ increases. Therefore, when generated under close proximity and with Coulombic interactions, the initially formed excitons would further bind into biexcitons. From the relative red-shift from PL to ASE emission, the biexcitonic binding energy (E_{xx}^{B}) was determined to be ca. 70 meV; sufficiently far above the room temperature thermal energy of k_BT ~26 meV. One of the main advantages of the high E_{xx}^{B} is that it limits the detrimental reabsorption losses, which contribute to less stringent conditions to achieve the necessary population inversion needed for amplification.[53] The additional consequence of the higher biexcitonic binding energy (at a fixed pump fluence), may lead to increased long term sustainability of device operation, which is very promising for the fabrication of stable and luminescent optoelectronic devices such as LEDs and lasers.

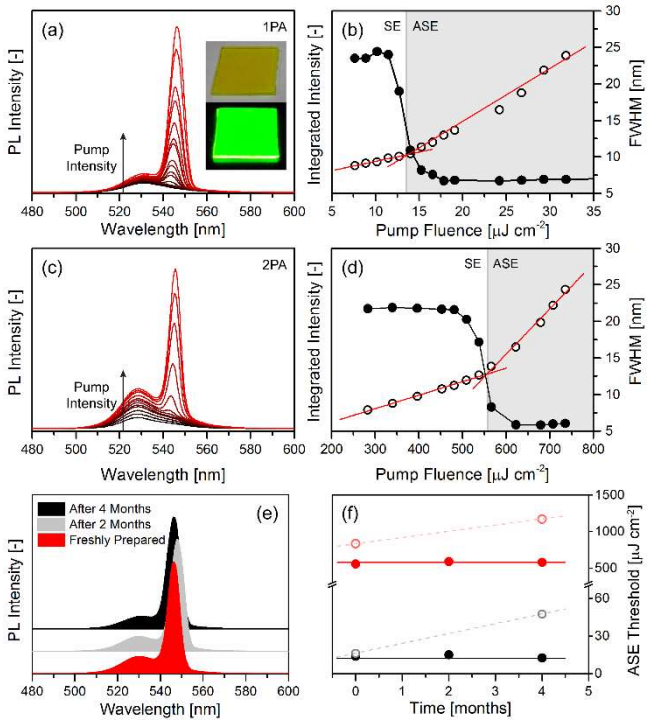

Figure 2. SE to ASE characteristics and photostability of dropcasted $CH_3NH_3PbBr_3$ NC thin films prepared with BnOH. **(a,c)** steady-state PL emission spectra excited using 400 nm (1PA) and 800 nm (2PA) pump pulses (150 fs, 1 kHz), with increasing laser fluence to approximately 38 and 760 μJ cm^{-2}, respectively. Inset in (a) photographs of dropcasted thin film on Quartz under ambient light (top) and under UV illumination (λ = 365 nm). **(b,d)** Spectrally integrated PL emission intensity (open circles) and FWHM (closed circles) as a function of laser pump fluence, respectively; the grey area represents the ASE regime. **(e)** Consistency of steady-state PL and ASE peak position above the ASE threshold of a freshly prepared (red), two-month old (grey), and four-month old (black) sample stored under ambient conditions (400 nm excitation; fluence 38 μJ cm^{-2}), and **(f)** corresponding ASE threshold values for 1PA (black) and 2PA (red) excitation, respectively. As a reference the corresponding values of the control samples are also presented (open circles).

Besides steady-state PL characterization, we also employed time-resolved PL (TRPL) measurements to investigate whether the origins of excitonic recombination and carrier life-times were altered upon BnOH addition. **Figure 3a** shows the PL spectrum integrated over the time window of the streak camera's spectrogram image (Figure 3b) when excited above the ASE threshold (i.e. 25 μJ cm^{-2}), where two emission peaks are clearly evident. The long-lived green component at ca. 525 nm (denoted SE) belongs to the excitonic PL emission, while the dominant short-lived component, attributed to biexcitonic ASE emission (i.e. red oval; denoted ASE) showed significantly higher intensity. To understand and compare the aforementioned SE and ASE dynamics in Figure 3b, the PL life-times of both were monitored in the picosecond regime. The life-times of the long-lived PL emission (SE) were obtained from a bi-exponential fit. The first

component with a 38.5 ps life-time is dominated by Auger recombination, due to the high pump fluence used. The much longer second life-time related to excitonic PL from spontaneous emission is estimated to be around 25 ns (based on a separate TRPL measurement taken over a longer time window). The ASE component, as shown in Figure 3c, reveals an even shorter lifetime (~10 ps), which is limited by the temporal resolution of our streak camera. We note that biexciton buildup is much faster compared to Auger recombination, and therefore outcompetes it. As a result, the non-radiative loss channel does not hinder the gain process significantly, and clearly allows for such low ASE thresholds to be observed in our samples.

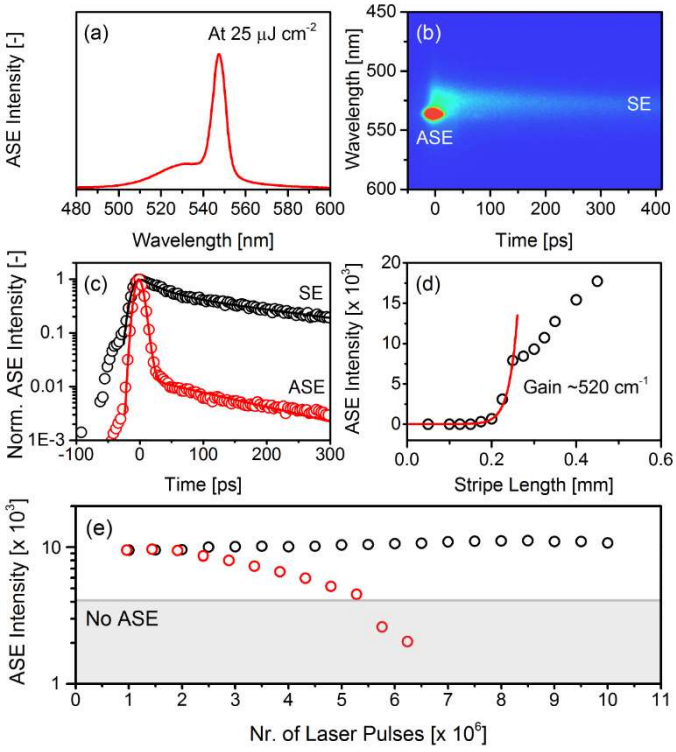

Figure 3. (a) PL spectrum integrated over the time window of the streak camera's spectrogram image in (b), **(b)** time-resolved PL spectra displaying the rise of a short-lived emission (red oval) as compared to the longer-lived PL component (light-blue tail), and **(c)** comparison of the PL life-times (circles) and fits (solid lines) of both SE and ASE contributions in (b), **(d)** variable stripe

length (VSL) measurement to determine to modal gain, and **(e)** laser pulse-dependent stability of a dropcasted $CH_3NH_3PbBr_3$ NC film prepared with BnOH (black circles) and in absence of BnOH (red circles; control). All spectra were excited using 400 nm (150 fs; 1 kHz) pump pulses at 25 μJ cm^{-2} laser fluence. Fit in (d) according to: $I_{ASE}(L) = (A/g)[e^{gL}-1]$.

Additionally, the optical gain of our $CH_3NH_3PbBr_3$ NC films was determined by employing a direct measurement known as variable stripe length (VSL) method, first developed by Shaklee and Leheny.[54] Under a constant fluence of 25 μJ cm^{-2} (i.e. above ASE threshold), the slit width was varied to produce a different excitation stripe length across the sample (Figure 3d). Here, the slit opening was placed at the center of the focused excitation stripe to ensure its central position within the slowly varying approximation along the excitation stripe (assuming a Gaussian profile for the excitation laser). The exponential fit in Figure 3d is derived from Shaklee and Leheny,[54] according to: $I_{ASE}(L) = (A/g)[e^{gL}-1]$, where I_{ASE} represents the integrated PL intensity collected from the ASE profile, A the cross-sectional excited area mapped by the penetration depth, L the (varied) excitation stripe length, and g the gain parameter we are interested in. The gain determined as ca. 520 cm^{-1}, which is among the highest recorded values under low pump fluence,[20] and significantly higher than conventional chalcogenide QDs (e.g. CdSe) which show much poorer gain performance. To further validate the robustness of our NC thin films, we assessed the photostability under continuous excitation under ambient conditions at 400 nm excitation and 25 μJ cm^{-2} pump fluence (repetition rate 1 kHz). As shown in Figure 3e, the integrated ASE peak intensity remains virtually unchanged after 10^7 laser pulses, equivalent to approximately 3 h of continuous pumping. Comparatively, the $CH_3NH_3PbBr_3$ NCs are significantly more stable than samples synthesized in absence of BnOH and conventional colloidal QDs.[55-57] Indeed, the former

already displayed a gradual intensity loss after only $2x10^6$ pulses, with a dramatic loss of ASE after ca. $5x10^6$ pulses (equivalent to approx. 1.5 h of continuous pumping). The outstanding photostability, optical gain properties, high PLQY, and low ASE thresholds thus place our NCs prepared with BnOH competitively with the best-in-class (perovskite) optoelectronic materials, and we believe that our NCs can find potential applications as suitable gain medium in whispering gallery mode (WGM) lasing or electrically-pumped Fabry-Pérot (FP) lasing for strong coherent light emission. The former was recently demonstrated by Wang et al. for all-inorganic $CsPbBr_3$ NCs.[19] By exploiting the versatility of 3D perovskites to tune the PL emission across the visible spectrum, our described synthesis may be further extended to lasing applications in the orange/red spectral region (i.e. $CH_3NH_3PbBr_{3-x}I_x$ NCs formed through anion-exchange or direct synthesis with I^-), see **Figure S9**).

So far, we have observed superior photophysical properties and improved structural stability for the NCs prepared with BnOH. Remarkably, the chemical composition from XPS and crystallographic structure and size distribution of the NCs are very similar to the control samples. So, how can these striking differences be explained? We hypothesize that BnOH could influence the ligand landscape and binding motifs on the NC surface, by (1) acting as a passivating ligand itself,[42] (2) influencing the binding modes of the OAc and OctAm ligands on the NC surface, or (3) both. To this end, we employed solid-state nuclear magnetic resonance (ssNMR), Fourier-transform infrared (FTIR) spectroscopy, and Raman spectroscopy (RS) in an attempt to elucidate the aforementioned hypotheses. The presence of the mono-substituted aromatic ring in BnOH (and toluene for that matter) is expected to give rise to a very strong absorption band at 700-750 cm^{-1} in FTIR (**Figure S10; Table S1**). Since this band was not detected, we believe that BnOH is not present on the NC surface, and therefore does not act as a ligand during the NC formation.

Likewise, no absorption from toluene was found at 700-750 cm^{-1} in the control samples, indicating that the tested samples were sufficiently purified and dried after synthesis. The inactivity as ligand is consistent with the HSAB theory (HSAB: hard soft acid base), which predicts that stronger chemical bonds are formed between acids and bases of similar softness/hardness. In our reaction, the bond between Pb^{2+} (borderline acid) and COO^- (from OAc; borderline base) is more favorable to form than between Pb^{2+} and BnOH, which acts as a hard base. Moreover, the BnOH is more unlikely to deprotonate and act as a Lewis base, since its pKa value (~15.4) is much higher than that of OAc (~8-8.5). The absence of ν(C=O) from the carboxylic acid at 1709 cm^{-1} in FTIR, and the concomitant presence of asymmetric stretching ν(COO^-) between 1500 and 1620 cm^{-1} (**see Figure S10**),[58] further confirms that all OAc is deprotonated and present as oleate on the NC surface. X-ray photoelectron spectroscopy (XPS) was employed to provide a more detailed analysis of the carboxylate binding on the NC surface (**Figure S11**). In particular, the O1s spectra revealed a clear distinction of two carboxylate oxygen atoms with different chemical surroundings, notably at ~530.1 eV (peak I; grey) and ~531.1 eV (peak III; blue), **see Figure 4a,b**. We postulate that these peaks are associated with the bidentate chelating and monodentate binding modes of the carboxylate on the NC surface, respectively (Figure 4c). The lower binding energy (B.E.) of the bidentate binding mode is considered to originate from the smaller distance of the oxygen atoms to the NC surface, due to increased screening by the electrons in the metal. On the other hand, we associate the signal at ~532.0 eV (peak II; red) to adsorbed OH-groups from water during sample preparation and handling under ambient conditions (50% RH). From the O1s spectra we can clearly deduce that the samples prepared with BnOH only show a single contribution of Pb-O-C bonds at ~530.1 eV; thus implying that the bound carboxylates cover the NC surface solely via bidentate chelating binding modes (Figure 4c). Conversely, the control samples show an additional

contribution at ~531.1 eV (peak III), which we believe is related to an unbound carboxylate group O=C-O-Pb of a monodentate binding mode (we cannot distinguish between the O=C-O-Pb and the Pb-O-C modes of the mono- and bidentate binding modes, respectively). The mixed carboxylate binding affects the packing density of the ligands on the NC surface (i.e. lower packing density), which will mostly manifest itself in the nonlinear optical absorption cross-sections, and thus the 2PA threshold value.[59] This is corroborated by the higher 2PA threshold for the control samples compared to BnOH-treated samples (Figure 2f). Moreover, a bidentate chelating binding mode provides stronger passivation of surface Pb atoms, thereby increasing the structural stability (Figure 2f and Figure 3e) while reducing the number of potential surface traps. Next, ssNMR (Figure 4d,e) was employed to further probe the chemical environment of the surface ligands. Similar to FTIR, the aromatic ring resonance of BnOH at δ ~7.3 ppm (^{1}H) was not detected, while the signal at δ ~127 ppm (^{13}C) cannot be distinguished from the C=C bond of OAc as both overlap. Notwithstanding, two signals in the spectra, however, could be exclusively assigned to oleic acid (signal '2'; δ ~23.3 ppm) and octylamine (signal 'α'; δ ~42.8 ppm). Both signals displayed a shift to higher electron density (Δδ -1.40 ppm; shielding) and lower electron density (Δδ +0.45 ppm; deshielding), respectively. These shifts may be seen in view of the deprotonation (COO^-) and protonation (NH_3^+) of both OAc and OctAm, as discussed previously. The ^{1}H ssNMR spectra exhibited broad peaks, typical for strongly bound ligands (i.e. with reduced mobility over the NC surface), and slightly shifted resonances, similar to the ^{13}C spectra. For both OctAm and OAc ligands, the terminal -CH_3 (signal '5' and 'β') are anticipated to give a signal at δ ~0.88 ppm. Since we expect similar shielding/deshielding resonance shifts in the ^{1}H spectra, the signals at δ ~0.73 ppm (Δδ -0.15 ppm) and δ ~1.13 ppm (Δδ +0.25 ppm) were therefore assigned to deprotonated OAc and protonated OctAm, respectively. The latter resonance is confirmed with the broad

terminal -CH_3 resonance of protonated octylammonium bromide (OABr) at δ ~1.20 ppm. Likewise, the broad signal 'γ' of the protonated amine -NH_3^+ in OABr at δ ~7.9 ppm is also present in our samples. A similar binding motif is also observed for $CsPbX_3$ NCs, where protonated oleylamine bromide acts as a ligand via hydrogen bonding.[60] Interestingly, the samples prepared with BnOH show a higher intensity of resonance 'β' compared to resonance '5', signifying a much larger concentration of protonated amine on the NC surface than the control sample, which is advantageous for achieving high PLQY.[60] The increased concentration of OctAm was further verified by Raman spectra (**Figure S12; Table S2**). In particular, the stronger rocking signal $r(NH_3)^+$ of protonated OctAm at 1201 cm^{-1} compared to the stretching ν(C-N) and twisting of τ(C-N) of $CH_3NH_3^+$ at 967 and 1581 cm^{-1}, respectively.[61] For the control sample, however, $r(NH_3)^+$ and stretching ν(C-N) show equal intensity. Similarly, the large intensity difference of OctAm stretching ν(N-H) at 3380 cm^{-1} also suggests a much higher concentration of amine on the NC surface. The different ligand concentrations and binding motifs on the NC surface thus attribute to the high PLQY, lower surface trap densities, and increased structural stability of the NCs.

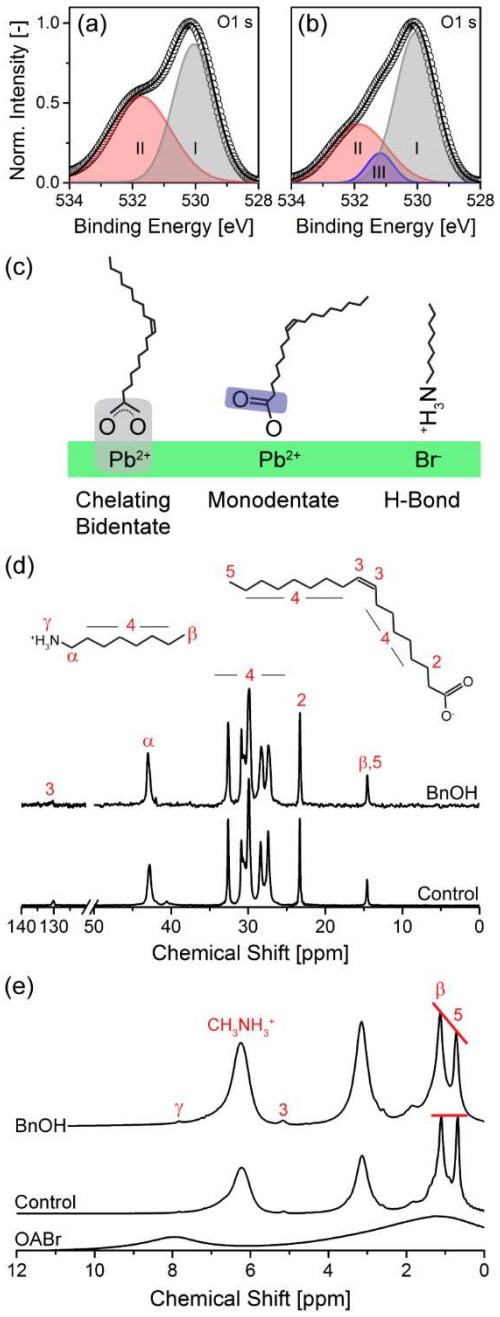

Figure 4. Spectroscopic analysis of $CH_3NH_3PbBr_3$ NCs prepared with BnOH / in absence of BnOH to determine the different ligand binding modes on the NC surface. **(a,b)** O1s X-ray photoelectron spectra of the BnOH and control samples, respectively. Here, peak I (grey) and III (blue) correspond to the bidentate bridging and monodentate binding modes of the carboxylic acid depicted in (c), whereas peak II (red) is related to –OH from water during sample preparation and

handling. **(c)** Schematic representation of the different carboxylate ligand binding modes on the NC surface, including OctAm binding to surface bromide atoms via hydrogen bonding. **(d)** ^{13}C solid-state NMR spectra, and **(e)** ^{1}H solid-state NMR spectra.

In conclusion, we have demonstrated that the addition of benzyl alcohol during the LARP synthesis favorably affects the structural and photophysical properties of the resultant $CH_3NH_3PbBr_3$ NCs. The benzyl alcohol plays a crucial role in the ligands binding motifs on the NC surface, thereby improving the surface-trap passivation and increasing the PLQY to near-unity values. This effectively resulted in very stable NCs and NC thin films (>4 months under ambient conditions), exhibiting near-unity PLQY, high optical gain (520 cm^{-1}), and ultralow ASE thresholds of ca. 13.9 and 569.7 μJ cm^{-2} at one-photon (400 nm) and two-photon (800 nm) excitation, respectively. The latter signifies a 5-fold improvement of the lowest reported nonlinear ASE threshold reported for perovskite NCs. The superior stability (both structurally and under continuous illumination), in combination with the low thresholds, render our NCs are ideal candidates for low-threshold lasing and other light-emitting applications.

ASSOCIATED CONTENT

Supporting Information. Materials and methods, optical and structural characterization of $CH_3NH_3PbBr_3$ NCs during purification, prepared with different ligands, and control samples. Thermogravimetric analysis, fluence-dependent PL, Z-scan, color tuning, FTIR, XPS, and Raman spectroscopy. The following files are available free of charge (pdf).

AUTHOR INFORMATION

Corresponding Author

*Subodh@ntu.edu.sg and tzechien@ntu.edu.sg

Author Contributions

The manuscript was written through contributions of all authors. All authors have given approval to the final version of the manuscript. ‡S.A.V. and Y.K.E.T. contributed equally to this work.

Notes

The authors declare no competing financial interest.

ACKNOWLEDGMENT

This research is supported by the National Research Foundation, Prime Minister's Office, Singapore under its Competitive Research Programme (CRP Award No. NRF-CRP14-2014-03). S.A.V. and Y.K.E.T. would like to thank Dr. Chen Shi for his assistance with X-ray photoelectron spectroscopy measurements. T.C.S. would like to acknowledge the financial support from the Ministry of Education Academic Research Fund Tier 1 Grants RG101/15 and RG173/16, and Tier 2 Grants MOE2015-T2-2-015 and MOE2016-T2-1-034.

REFERENCES

1. NREL. *https://www.nrel.gov/pv/assets/images/efficiency-chart.png* **(Last viewed 14-03-2017)**.

2. Saliba, M.; Matsui, T.; Seo, J.-Y.; Domanski, K.; Correa-Baena, J.-P.; Nazeeruddin, M. K.; Zakeeruddin, S. M.; Tress, W.; Abate, A.; Hagfeldt, A.; Gratzel, M. *Energy Environ. Sci.* **2016,** 9, 1989-1997.

3. Tan, Z. K.; Moghaddam, R. S.; Lai, M. L.; Docampo, P.; Higler, R.; Deschler, F.; Price, M.; Sadhanala, A.; Pazos, L. M.; Credgington, D.; Hanusch, F.; Bein, T.; Snaith, H. J.; Friend, R. H. *Nat. Nanotechnol.* **2014,** 9, 687-692.

4. Cho, H.; Jeong, S.-H.; Park, M.-H.; Kim, Y.-H.; Wolf, C.; Lee, C.-L.; Heo, J. H.; Sadhanala, A.; Myoung, N.; Yoo, S.; Im, S. H.; Friend, R. H.; Lee, T.-W. *Science* **2015,** 350, 1222-1225.

5. Kim, Y. H.; Cho, H.; Heo, J. H.; Kim, T. S.; Myoung, N.; Lee, C. L.; Im, S. H.; Lee, T. W. *Adv. Mater.* **2015,** 27, 1248-1254.

6. Wang, N.; Cheng, L.; Ge, R.; Zhang, S.; Miao, Y.; Zou, W.; Yi, C.; Sun, Y.; Cao, Y.; Yang, R.; Wei, Y.; Guo, Q.; Ke, Y.; Yu, M.; Jin, Y.; Liu, Y.; Ding, Q.; Di, D.; Yang, L.; Xing, G.; Tian, H.; Jin, C.; Gao, F.; Friend, R. H.; Wang, J.; Huang, W. *Nat. Photonics* **2016,** 10, 699-704.

7. Li, J.; Shan, X.; Bade, S. G. R.; Geske, T.; Jiang, Q.; Yang, X.; Yu, Z. *J. Phys. Chem. Lett.* **2016,** 7, 4059-4066.

8. Chih, Y.-K.; Wang, J.-C.; Yang, R.-T.; Liu, C.-C.; Chang, Y.-C.; Fu, Y.-S.; Lai, W.-C.; Chen, P.; Wen, T.-C.; Huang, Y.-C.; Tsao, C.-S.; Guo, T.-F. *Adv. Mater.* **2016,** 28, 8687-8694.

9. Kim, Y.-H.; Wolf, C.; Kim, Y.-T.; Cho, H.; Kwon, W.; Do, S.; Sadhanala, A.; Park, C. G.; Rhee, S.-W.; Im, S. H.; Friend, R. H.; Lee, T.-W. *ACS Nano* **2017,** 11, 6586-6593.

10. Xing, G.; Mathews, N.; Lim, S. S.; Yantara, N.; Liu, X.; Sabba, D.; Grätzel, M.; Mhaisalkar, S.; Sum, T. C. *Nat. Mater.* **2014,** 13, 476-480.

11. Xing, J.; Liu, X. F.; Zhang, Q.; Ha, S. T.; Yuan, Y. W.; Shen, C.; Sum, T. C.; Xiong, Q. *Nano Lett.* **2015,** 15, 4571-4577.

12. Zhu, H.; Fu, Y.; Meng, F.; Wu, X.; Gong, Z.; Ding, Q.; Gustafsson, M. V.; Trinh, M. T.; Jin, S.; Zhu, X. Y. *Nat. Mater.* **2015,** 14, 636-642.

13. Eaton, S. W.; Lai, M.; Gibson, N. A.; Wong, A. B.; Dou, L.; Ma, J.; Wang, L.-W.; Leone, S. R.; Yang, P. *Proc. Natl. Acad. Sci.* **2016,** 113, 1993-1998.

14. Dou, L.; Yang, Y.; You, J.; Hong, Z.; Chang, W.-H.; Li, G.; Yang, Y. *Nat. Commun.* **2014,** 5, 5404.

15. Akkerman, Q. A.; D'Innocenzo, V.; Accornero, S.; Scarpellini, A.; Petrozza, A.; Prato, M.; Manna, L. *J. Am. Chem. Soc.* **2015,** 137, 10276-10281.

16. Protesescu, L.; Yakunin, S.; Bodnarchuk, M. I.; Krieg, F.; Caputo, R.; Hendon, C. H.; Yang, R. X.; Walsh, A.; Kovalenko, M. V. *Nano Lett.* **2015,** 15, 3692-3696.

17. Nedelcu, G.; Protesescu, L.; Yakunin, S.; Bodnarchuk, M. I.; Grotevent, M. J.; Kovalenko, M. V. *Nano Lett.* **2015,** 15, 5635-5640.

18. Pan, J.; Sarmah, S. P.; Murali, B.; Dursun, I.; Peng, W.; Parida, M. R.; Liu, J.; Sinatra, L.; Alyami, N.; Zhao, C.; Alarousu, E.; Ng, T. K.; Ooi, B. S.; Bakr, O. M.; Mohammed, O. F. *J. Phys. Chem. Lett.* **2015,** 6, 5027-5033.

19. Wang, Y.; Li, X.; Song, J.; Xiao, L.; Zeng, H.; Sun, H. *Adv. Mater.* **2015,** 27, 7101-7108.

20. Yakunin, S.; Protesescu, L.; Krieg, F.; Bodnarchuk, M. I.; Nedelcu, G.; Humer, M.; De Luca, G.; Fiebig, M.; Heiss, W.; Kovalenko, M. V. *Nat. Commun.* **2015,** 6, 8056.

21. Priante, D.; Dursun, I.; Alias, M. S.; Shi, D.; Melnikov, V. A.; Ng, T. K.; Mohammed, O. F.; Bakr, O. M.; Ooi, B. S. *Appl. Phys. Lett.* **2015,** 106.

22. Vybornyi, O.; Yakunin, S.; Kovalenko, M. V. *Nanoscale* **2016,** 8, 6278-6283.

23. Protesescu, L.; Yakunin, S.; Bodnarchuk, M. I.; Bertolotti, F.; Masciocchi, N.; Guagliardi, A.; Kovalenko, M. V. *J. Am. Chem. Soc.* **2016,** 138, 14202-14205.

24. Protesescu, L.; Yakunin, S.; Kumar, S.; Bär, J.; Bertolotti, F.; Masciocchi, N.; Guagliardi, A.; Grotevent, M.; Shorubalko, I.; Bodnarchuk, M. I.; Shih, C.-J.; Kovalenko, M. V. *ACS Nano* **2017,** 11, 3119-3134.

25. Xing, G.; Kumar, M. H.; Chong, W. K.; Liu, X.; Cai, Y.; Ding, H.; Asta, M.; Grätzel, M.; Mhaisalkar, S.; Mathews, N.; Sum, T. C. *Adv. Mater.* **2016,** 28, 8191-8196.

26. Milot, R. L.; Eperon, G. E.; Green, T.; Snaith, H. J.; Johnston, M. B.; Herz, L. M. *J. Phys. Chem. Lett.* **2016,** 7, 4178-4184.

27. Schmidt, L. C.; Pertegás, A.; González-Carrero, S.; Malinkiewicz, O.; Agouram, S.; Mínguez Espallargas, G.; Bolink, H. J.; Galian, R. E.; Pérez-Prieto, J. *J. Am. Chem. Soc.* **2014,** 136, 850-853.

28. Zhang, F.; Zhong, H.; Chen, C.; Wu, X. G.; Hu, X.; Huang, H.; Han, J.; Zou, B.; Dong, Y. *ACS Nano* **2015,** 9, 4533-4542.

29. Gonzalez-Carrero, S.; Francés-Soriano, L.; González-Béjar, M.; Agouram, S.; Galian, R. E.; Pérez-Prieto, J. *Small* **2016,** 12, 5245-5250.

30. Shamsi, J.; Abdelhady, A. L.; Accornero, S.; Arciniegas, M.; Goldoni, L.; Kandada, A. R. S.; Petrozza, A.; Manna, L. *ACS Energy Lett.* **2016,** 1, 1042-1048.

31. Akkerman, Q. A.; Gandini, M.; Di Stasio, F.; Rastogi, P.; Palazon, F.; Bertoni, G.; Ball, J. M.; Prato, M.; Petrozza, A.; Manna, L. *Nat. Energy* **2016,** 2, 16194.

32. Bekenstein, Y.; Koscher, B. A.; Eaton, S. W.; Yang, P.; Alivisatos, A. P. *J. Am. Chem. Soc.* **2015,** 137, 16008–16011.

33. Cho, J.; Choi, Y.-H.; O'Loughlin, T. E.; De Jesus, L.; Banerjee, S. *Chem. Mater.* **2016,** 28, 6909-6916.

34. Ling, Y.; Yuan, Z.; Tian, Y.; Wang, X.; Wang, J. C.; Xin, Y.; Hanson, K.; Ma, B.; Gao, H. *Adv. Mater.* **2015,** 28, 305–311.

35. Bhaumik, S.; Veldhuis, S. A.; Ng, Y. F.; Li, M.; Muduli, S. K.; Sum, T. C.; Damodaran, B.; Mhaisalkar, S.; Mathews, N. *Chem. Commun.* **2016,** 52, 7118-7121.

36. McMeekin, D. P.; Sadoughi, G.; Rehman, W.; Eperon, G. E.; Saliba, M.; Hörantner, M. T.; Haghighirad, A.; Sakai, N.; Korte, L.; Rech, B.; Johnston, M. B.; Herz, L. M.; Snaith, H. J. *Science* **2016,** 351, 151-155.

37. Li, G.; Tan, Z. K.; Di, D.; Lai, M. L.; Jiang, L.; Lim, J. H. W.; Friend, R. H.; Greenham, N. C. *Nano Lett.* **2015,** 15, 2640-2644.

38. Huang, S.; Li, Z.; Kong, L.; Zhu, N.; Shan, A.; Li, L. *J. Am. Chem. Soc.* **2016,** 138, 5749-5752.

39. Luo, B.; Pu, Y.-C.; Lindley, S. A.; Yang, Y.; Lu, L.; Li, Y.; Li, X.; Zhang, J. Z. *Angew. Chem. Int. Ed.* **2016,** 55, 8864-8868.

40. Sun, C.; Zhang, Y.; Ruan, C.; Yin, C.; Wang, X.; Wang, Y.; Yu, W. W. *Adv. Mater.* **2016,** 28, 10088-10094.

41. Niederberger, M.; Pinna, N., *Metal Oxide Nanoparticles in Organic Solvents: Synthesis, Formation, Assembly and Application*. Springer-Verlag London: 2009.

42. Veldhuis, S. A.; Vijselaar, W. J. C.; Stawski, T. M.; ten Elshof, J. E. *Inorg. Chem.* **2014,** 53, 13188-13196.

43. Baikie, T.; Barrow, N. S.; Fang, Y.; Keenan, P. J.; Slater, P. R.; Piltz, R. O.; Gutmann, M.; Mhaisalkar, S. G.; White, T. J. *J. Mater. Chem. A* **2015,** 3, 9298-9307.

44. Tong, Y.; Bladt, E.; Aygüler, M. F.; Manzi, A.; Milowska, K. Z.; Hintermayr, V. A.; Docampo, P.; Bals, S.; Urban, A. S.; Polavarapu, L.; Feldmann, J. *Angew. Chem. Int. Ed.* **2016,** 55, 13887-13892.

45. Dang, C.; Lee, J.; Breen, C.; Steckel, J. S.; Coe-Sullivan, S.; Nurmikko, A. *Nat. Nanotechnol.* **2012,** 7, 335-339.

46. García-Santamaría, F.; Chen, Y.; Vela, J.; Schaller, R. D.; Hollingsworth, J. A.; Klimov, V. I. *Nano Lett.* **2009,** 9, 3482-3488.

47. Klimov, V. I.; Ivanov, S. A.; Nanda, J.; Achermann, M.; Bezel, I.; McGuire, J. A.; Piryatinski, A. *Nature* **2007,** 447, 441-446.

48. Moreels, I.; Rainò, G.; Gomes, R.; Hens, Z.; Stöferle, T.; Mahrt, R. F. *Adv. Mater.* **2012,** 24, OP231-OP235.

49. Wang, Y.; Li, X.; Zhao, X.; Xiao, L.; Zeng, H.; Sun, H. *Nano Lett.* **2016,** 16, 448-453.

50. Yang, B.; Mao, X.; Yang, S.; Li, Y.; Wang, Y.; Wang, M.; Deng, W.; Han, K. *ACS Appl. Mater. Interfaces* **2016,** 8, 19587-19592.

51. Sheik-Bahae, M.; Said, A. A.; Wei, T.-H.; Hagan, D. J.; Stryland, E. W. V. *IEEE J. Quantum Electron.* **1990,** 26, 760-769.

52. Larson, D. R.; Zipfel, W. R.; Williams, R. M.; Clark, S. W.; Bruchez, M. P.; Wise, F. W.; Webb, W. W. *Science* **2003,** 300, 1434-1436.

53. Grim, J. Q.; Christodoulou, S.; Di Stasio, F.; Krahne, R.; Cingolani, R.; Manna, L.; Moreels, I. *Nat. Nanotechnol.* **2014,** 9, 891-895.

54. Shaklee, K. L.; Leheny, R. F. *Appl. Phys. Lett.* **1971,** 18, 475-477.

55. Peng, X.; Schlamp, M. C.; Kadavanich, A. V.; Alivisatos, A. P. *J. Am. Chem. Soc.* **1997,** 119, 7019-7029.

56. Guzelturk, B.; Kelestemur, Y.; Olutas, M.; Delikanli, S.; Demir, H. V. *ACS Nano* **2014,** 8, 6599-6605.

57. Xing, G.; Liao, Y.; Wu, X.; Chakrabortty, S.; Liu, X.; Yeow, E. K. L.; Chan, Y.; Sum, T. C. *ACS Nano* **2012,** 6, 10835-10844.

58. Lin-Vien, D.; Colthup, N. B.; Fateley, W. G.; Grasselli, J. G., *The Handbook of Infrared and Raman Characteristic Frequencies of Organic Molecules*. Academic Press: San Diego, 1991; p 1-503.

59. Chen, W.; Bhaumik, S.; Veldhuis, S. A.; Xing, G.; Xu, Q.; Grätzel, M.; Mhaisalkar, S.; Mathews, N.; Sum, T. C. *Nat. Commun.* **2017,** 8, 15198.

60. De Roo, J.; Ibáñez, M.; Geiregat, P.; Nedelcu, G.; Walravens, W.; Maes, J.; Martins, J. C.; Van Driessche, I.; Kovalenko, M. V.; Hens, Z. *ACS Nano* **2016,** 10, 2071-2081.

61. Xie, L.-Q.; Zhang, T.-Y.; Chen, L.; Guo, N.; Wang, Y.; Liu, G.-K.; Wang, J.-R.; Zhou, J.-Z.; Yan, J.-W.; Zhao, Y.-X.; Mao, B.-W.; Tian, Z.-Q. *Phys. Chem. Chem. Phys.* **2016,** 18, 18112-18118.

TOC GRAPHIC.

Ultralow amplified spontaneous emission thresholds and outstanding photostability of $CH_3NH_3PbBr_3$ nanocrystals is achieved through direct precipitation in a toluene/benzyl alcohol phase. The benzyl alcohol plays a pivotal role in steering the surface ligands' binding motifs on the NC surface, resulting in enhanced surface-trap passivation, near-unity PLQY, ultralow one- and two-photon ASE thresholds, and >4 months stability under ambient conditions.

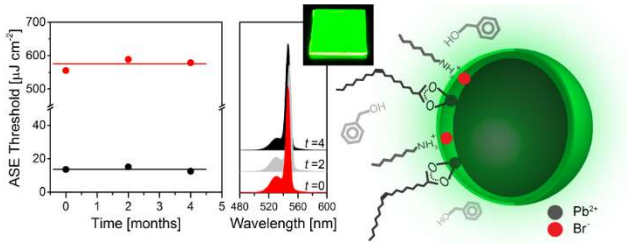

SUPPORTING INFORMATION

Benzyl Alcohol-treated $CH_3NH_3PbBr_3$ Nanocrystals Exhibiting High Luminescence, Stability and Ultralow Amplified Spontaneous Emission Thresholds

Sjoerd A. Veldhuis,[†] Yong Kang Eugene Tay,[‡] Annalisa Bruno,[†,‡] Sai S.H. Dintakurti,[†] Saikat Bhaumik,[†] Subas Kumar Muduli,[†] Mingjie Li,[‡] Nripan Mathews,[†,§] Tze Chien Sum[‡], and Subodh G. Mhaisalkar[†,§]**

[†]Energy Research Institute at NTU (ERI@N), Research Techno Plaza, X-Frontier Block Level 5, 50 Nanyang Drive, Singapore 637553, Singapore.

[‡]Division of Physics and Applied Physics, School of Physical and Mathematical Sciences, Nanyang Technological University, 21 Nanyang Link, Singapore 637371, Singapore.

[§]School of Materials Science and Engineering, Nanyang Technological University, 50 Nanyang Avenue, Singapore 639798.

*Corresponding Authors:

Subodh@ntu.edu.sg and Tzechien@ntu.edu.sg

Materials and Methods

Chemicals: Lead bromide, $PbBr_2$ (99.999%, trace metals basis), *n*-octylamine (OctAm; 99%), oleic acid (OAc; 90%), triethylamine (TEAm; 99%), *N,N*-dimethylformamide, (DMF; 99.8%), toluene (anhydrous, 99.7% GC), and benzyl alcohol (BnOH; 99.5%) were all purchased from Sigma-Aldrich. Methylammonium bromide (MABr) was acquired from Dyseol. All chemicals were used without further purification.

Synthesis of $CH_3NH_3PbBr_3$ NPs: A solution of $PbBr_2$ (0.2 mmol; 73.4 mg) and MABr (0.2 mmol; 22.4 mg) was prepared in 1 mL DMF. Subsequently, 150 µL of precursor solution was swiftly injected in a solution of 5 mL toluene, 20 µL OctAm, 1000 µL OAc, and 1000 µL benzyl alcohol (all added in this sequence) under vigorous stirring for 5 min. Due to the presence of BnOH, all NPs were directly precipitated, and a bright yellow/green suspension was obtained. All experiments were performed under ambient conditions at room temperature.

$CH_3NH_3PbBr_3$ NP Purification: The crude reaction mixture was transferred to a centrifuge tube for further purification. The NPs were centrifuged for 10 min at 6000 rpm. After centrifugation, the supernatant phase was discarded and the precipitated NPs were redispersed in 2 mL toluene. Then, 2 µL of pure amine (e.g. OctAm or TEAm) was added to the redispersed NPs and mixed with a vortex stirrer (at 2500 min^{-1}) for 120 s. The dispersion was then centrifuged again for 5 min at 8000 rpm. Unless stated otherwise, the precipitated NPs were used for further studies. All samples were stored and handled under ambient conditions (at 50% RH).

$CH_3NH_3PbBr_3$ Thin Film Deposition: The $CH_3NH_3PbBr_3$ nanocrystal films were dropcasted on Quartz substrates. In order to remove and residual solvent before optical characterization, the films were allowed to dry at room temperature under ambient conditions.

X-ray Diffraction: The crystal phase and lattice parameters of the synthesized NCs were determined using a Bruker D8 advance diffractometer with a 0D LynxEYE™ detector. Scans from 2θ = 5-40° were recorded (step sizes of 0.02° and 3 s per step) of thin films dropcasted on cleaned glass substrates.

Electron Microscopy: Selected samples were diluted in toluene, dropcasted on a Cu grid, and dried overnight in a drybox (<30% RH). Images were recorded using a Jeol JEM-2010 microscope operated at 200 kV.

Optical Absorption Spectroscopy: UV-vis spectra of diluted precipitate and supernatant solutions in toluene were collected using a Shimadzu UV-3600 spectrophotometer, from 300-800 nm with 0.2 nm steps (0.1 s integration time).

Fourier Transform Infrared: Attenuated total reflectance Fourier transform infrared (ATR-FTIR) measurements were performed using a Perkin Elmer Frontier, equipped with a Diamond ZnSe ATR crystal. Spectra were collected from 4000-600 cm^{-1} (32 scans; 2 cm^{-1} per step).

Raman spectroscopy: Raman spectra of dropcasted thin films on cleaned Quartz substrates were acquired in the range of 200-3500 cm^{-1} using a Renishaw Raman microscope configured with a CCD array detector. A laser (λ_{ex} = 785 nm) with a pump power <1 mW was used for excitation. The Raman spectra were collected by a Leica 1003 objective lens (NA = 50.85) with a frequency resolution of 0.7 cm^{-1} and 20 s (5 cycles) integration time.

X-ray photoelectron spectroscopy: XPS spectra were collected using a monochromatic X-ray source from Al Kα (hν = 1486.7 eV), equipped with a hemispherical analyzer (EA125, Omicron). Peak positions are based on a fixed C1s peak position of 285 eV for all spectra.

Photoluminescence Spectroscopy: Measurements on dilutions of precipitate and supernatant solutions in toluene were performed in Quartz cuvettes using a Horiba Fluoromax-4 spectrofluorometer at 350 nm laser excitation wavelength. For all spectra, the measured PL intensity was adjusted for the absorbance intensity at the excitation wavelength. Additional femtosecond optical spectroscopic methods were used to measure the ASE thresholds, TRPL, and PLQY. Here, the Coherent Libra regenerative amplifier (50 fs, 1 kHz, 800 nm) seeded by a Coherent Vitesse Oscillator (100 fs, 80 MHz), and the Coherent Legend Regenerative amplifier (150 fs, 1 kHz, 800 nm) seeded by a Coherent Vitesse Oscillator (100 fs, 80 MHz), were used as laser sources. The 800 nm excitation pulses for two-photon pump studies were generated from

the Coherent Libra Regenerative amplifier's output, whereas the 400 nm pulses (single-photon pump) were obtained by addition of a frequency doubling BBO crystal. The PL emission from the samples were collected at a backscattering angle of 150° by a collimating lens pair and guided into an optical fiber that was coupled to a spectrometer (Acton, SpectraPro 2500i) and detected by a charge coupled device (CCD; Princeton Instruments, Pixis 400B). Time-resolved PL (TRPL) was collected using an Optronis Optoscope streak camera system. The photoluminescence quantum yield (PLQY) of the perovskite thin-films were measured using an integrating sphere excited by a 405 nm continuous wave (CW) diode-pumped laser from Cobolt 06-MLD. The emissions were further corrected for the CCD and grating response via their corresponding response function. All optical measurements were performed under room temperature and ambient conditions.

Variable Stripe Length Measurements: Room temperature gain measurements were carried out via the variable stripe length (VSL) method using the BBO-doubled pump at 400 nm. The excitation stripe was obtained by passing the pump through a cylindrical lens (f = 20 cm) and its stripe length was varied through a fixated digital Vernier caliper in the middle of the stripe beam. The emission spectra were collected similarly to the PL measurements.

Z-scan Technique: The 2PA absorption cross-section was carried out via the Z-scan technique using the Coherent Libra's direct pulse at 800 nm. The excitation power is fixed and variation of fluence under similar pumping power was obtained by mounting the dilute colloidal solution (concentration approximately $5.83 \cdot 10^{-5}$ mol dm^{-3}) onto a mechanical stage mount with designated range of motion. The transmission spectra were collected using a homemade Lab-view program.

Solid-State Nuclear Magnetic Resonance: The Solid State NMR spectra were acquired on a 600 MHz Bruker Ascend magnet with Bruker AVANCE III controller and Topspin 3.5 software. A Bruker 4 mm magic angle spinning probe was used with ^{1}H and ^{13}C referenced to alanine. Powder samples were packed at the center of zirconia rotors using teflon filler and capped with Kel-F caps. The samples were spun at 12000 Hz at ambient temperature. The ^{1}H and ^{13}C

CPMAS spectra were collected for 64 and 128 scans, respectively, with a contact time of 5000 μs.

Nanocrystal purification and optical characterization

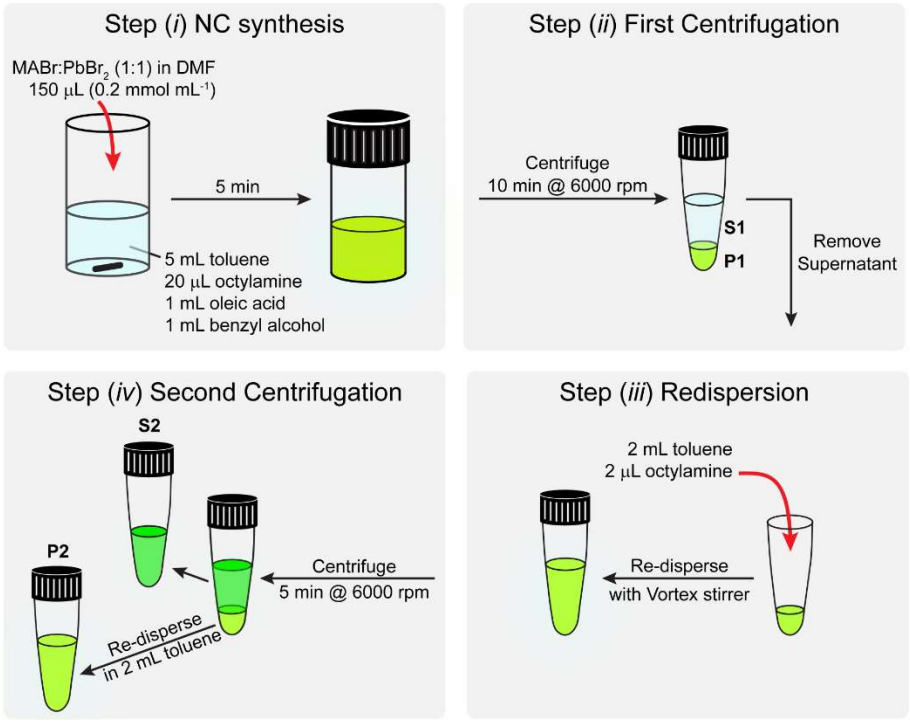

Figure S1. Schematic overview of $CH_3NH_3PbBr_3$ NCs synthesis, redispersion, and purification protocols.

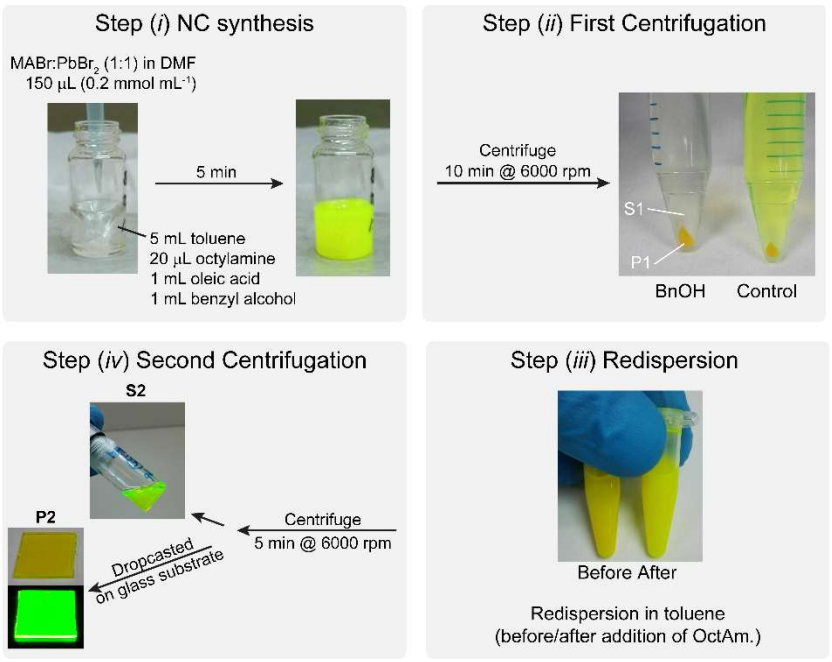

Figure S2. Photographs of $CH_3NH_3PbBr_3$ NCs synthesis, redispersion, and purification protocols.

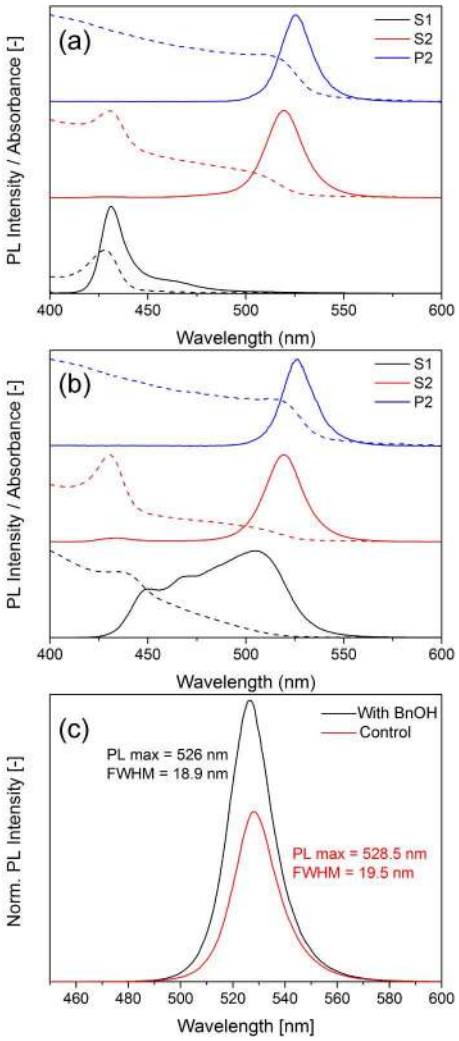

Figure S3. Absorbance and steady-state PL spectra of S1, S2, and P2 fractions during NC purification for reactions carried out **(a)** with BnOH, and **(b)** in absence of BnOH (control); where, 'S' and 'P' denote the supernatant and precipitate phases depicted in the purification protocol (see Figure S2). **(c)** Normalized PL spectra of precipitate fraction 'P2' indicates the use of BnOH during synthesis greatly enhances the photoluminescence intensity.

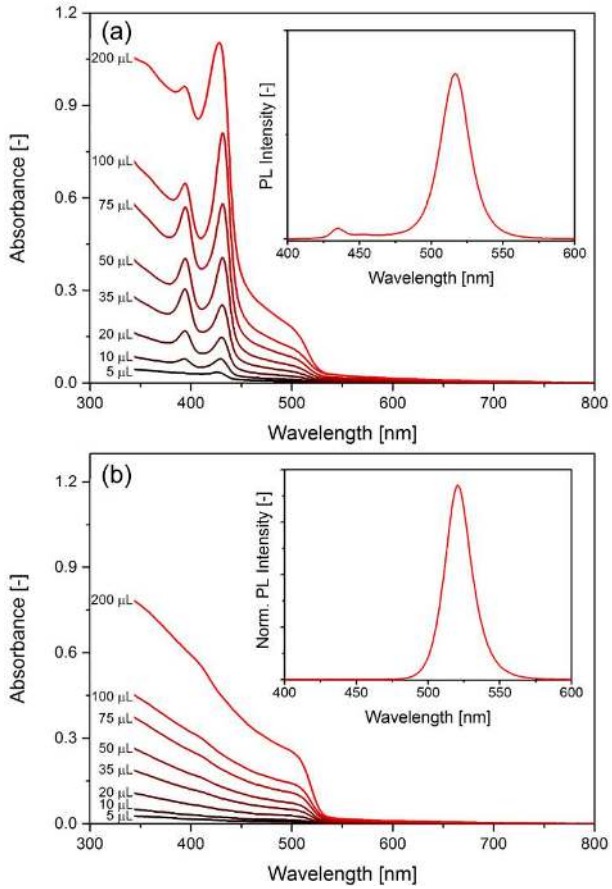

Figure S4. Absorption spectra for different concentrations of NP solution 'S2' with **(a)** OctAm, and **(b)** TEAm as ligands, respectively. The concentration ranges from 5-200 µL NC solution in 3 mL toluene. Insets: normalized PL spectra of a 20 µL NC solution (at 350 nm excitation). The strong excitonic absorption peaks in (a) at approximately 394 and 431 nm originates from the formation of a layered octylammonium lead bromide phase, $(OA)_2PbBr_4$, of single (n=1) and double (n=2) layered inorganic lead halide thickness, respectively. Despite the strong excitonic absorption, this phase shows negligible contribution to the overall PL intensity. Excess ligands, not contributing to the redispersion of the NCs may form the additional layered perovskite phase. To prove the latter, the OctAm ligand was replaced with the TEAm. Due to its branched nature, this ligand in incapable of forming a layered perovskite structure, and only band edge absorption and PL emission of the $CH_3NH_3PbBr_3$ were observed.

Structural characterization of control sample

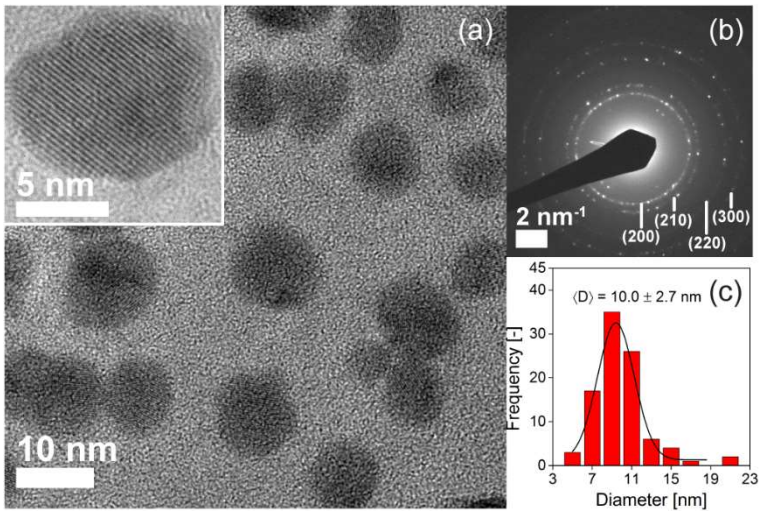

Figure S5. Structural characterization of $CH_3NH_3PbBr_3$ NCs prepared without BnOH (control). **(a)** HR-TEM image of an ensemble of $CH_3NH_3PbBr_3$ NCs. Inset: single NP at high magnification with clearly visible lattice fringes. **(b)** Electron diffraction pattern acquired from typical areas as shown in (a). **(c)** Particle size distribution calculated from at least 100 crystallites recorded at lower magnification.

Thermogravimetric analysis

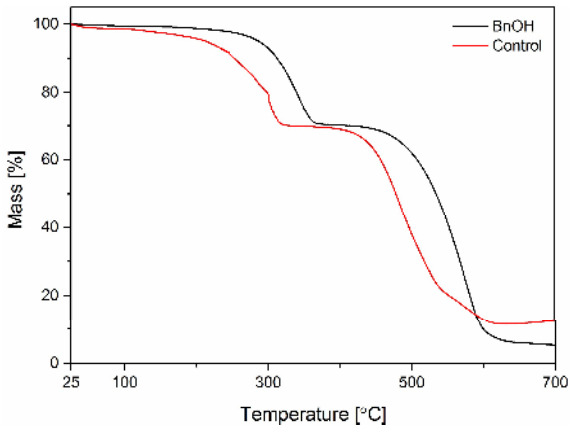

Figure S6. Thermogravimetric analysis of NCs prepared with (black) and in absence of (red) BnOH.

Excitonic Emission

Fluence-dependent time-resolved PL experiments were used to to validate the identity of the photoexcited carriers (i.e. free-carriers or excitons). In highly emissive materials, where radiative recombination dominates, the rate equation is $dN/dt = -k_r N^{\gamma}$. If the PL in our system is indeed excitonic in nature, we expect to fall within the monomolecular recombination regime (i.e. γ = 1). Since time-dependent PL is proportional to the rate of recombination, we assume: $I_{PL}(t=0) \propto N_0 \propto F$, where N_0 is the number of initially excited carriers (at t = 0), before any decay has occurred, and F the excitation fluence. As shown in **Figure S7**, our measurements show a linear relationship with a slope of ~1, thus confirming the excitonic nature of our PL emission. The samples were pumped at very low fluence (20-600 nJ cm^{-2}) to avoid any multi-particle effects.

In order to validate that the ASE onset stems from biexcitons, we first have to consider the possibility of excitonic ASE. In the case of NCs, in principle, there is a close balance between the absorption and stimulated emission rates within the $\langle N \rangle \sim 1$ regime (i.e. average of one exciton per NC). Hence, it is difficult to achieve optical amplification and lasing from single exciton gain in our system. This further implies that the stimulated emission only dominates when the NCs contain at least $\langle N \rangle \sim 2$ (i.e. biexcitons).

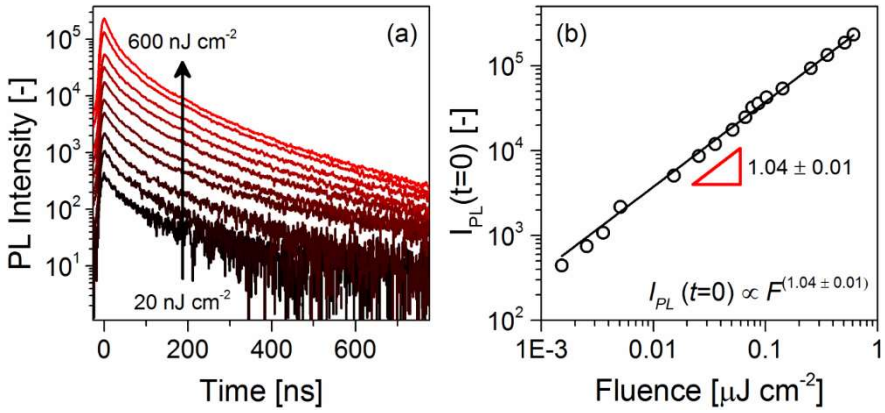

Figure S7. (a) Fluence-dependent TRPL measurement of the BnOH NCs in extremely low pump fluence regimes. **(b)** The log-log plot of TRPL peaks with respect to pumping fluences. The fitting reveals a linear relationship with a gradient of ~1, showing the excitonic nature of radiative recombination in our NCs.

Absorption Cross-sections

The one-/two-photon absorption cross-sections were measured in order to justify the obtained low ASE thresholds. A dilute colloidal $CH_3NH_3PbBr_3$ NC solution (conc. approximately $1.48 \cdot 10^{-5}$ mol dm^{-3}) in a 1 mm-thick cuvette was used for this purpose (i.e. in order to avoid re-absorption and scattering effects).

Firstly, the linear one-photon absorption cross-section $\sigma_{abs}^{(1)}$ was determined by tracing the time-dependent PL amplitudes as a function of the excitation fluence. This method of calculation was adopted by Ivanov et al. for traditional semiconducting chalcogenide QDs with quantum yields close to unity,[1] and was previously also used for halide perovskite NCs. We obtained a linear absorption cross-section in order of $\sigma_{abs}^{(1)} = (1.4 \pm 0.4) \cdot 10^{-13}$ cm^2, which is similar to reported values for fully inorganic $CsPbBr_3$ NCs,[2, 3] while several orders of magnitude higher than most inorganic chalcogenide QDs of similar size.[4]

The two-photon absorption cross-section was measured using the Z-scan technique,[5] which allows us to determine the sample's two-photon absorption coefficient β and in turn determine $\sigma_{abs}^{(2)}$ with the relation: $\sigma_{abs}^{(2)} = \frac{hc\beta}{\lambda C n_A}$. Following this, we obtained the two-photon absorption cross section of $\sigma_{abs}^{(2)} = (1.0 \pm 0.2) \cdot 10^5$ GM, where 1 GM = 10^{-50} cm^4 s. Generally, the large absorption cross-section and high quantum yields of our NCs are likely to be the underlying reasons for achieving the ultralow ASE thresholds.

Sheik-Bahae et al. (*IEEE J. Quantum Electron.* **1990**, 26, 760-769) derived the fitting parameters of the transmittance with respect to scan position z:

$$T(z) = \sum_{m=o}^{\infty} \frac{\left[\dfrac{-q_0}{1+\left(\dfrac{z-a}{z_0}\right)}\right]^m}{(m+1)^{1.5}} = 1 + \frac{\left(\dfrac{-q_0}{1+\left(\dfrac{z-a}{z_0}\right)}\right)}{(2)^{1.5}} + \frac{\left[\dfrac{-q_0}{1+\left(\dfrac{z-a}{z_0}\right)}\right]^2}{(3)^{1.5}} + \ldots.$$

Here, we only consider the first three terms and neglect the further terms. From the fit, we are able to obtain values of q_0 and z_0.

The peak laser pulse intensity can be calculated using a Gaussian beam approximation $I_0 = \dfrac{2P_0}{f_{rep}\left(\pi w_0^2\right)\tau_L\sqrt{\pi}}$, where P_0 is the excitation power, f_{rep} the pulse's repetition rate, and τ_L the laser pulse duration (~150fs). The beam waist w_0 can be calculated from the Rayleigh range z_0 from the fit, using $w_0 = \sqrt{\dfrac{\lambda z_0}{\pi}}$. With this, we are able to calculate the two-photon absorption coefficient β from the relationship $\beta = \dfrac{q_0}{I_0 L}$, where L is the thickness of the sample (i.e. 1 mm thin quartz cuvette). Lastly, the two-photon absorption cross section is calculated using the relation $\sigma_{abs}^{(2)} = \dfrac{hc\beta}{\lambda C n_A}$, where C is the colloidal sample's concentration and N_A is the Avogadro's constant.

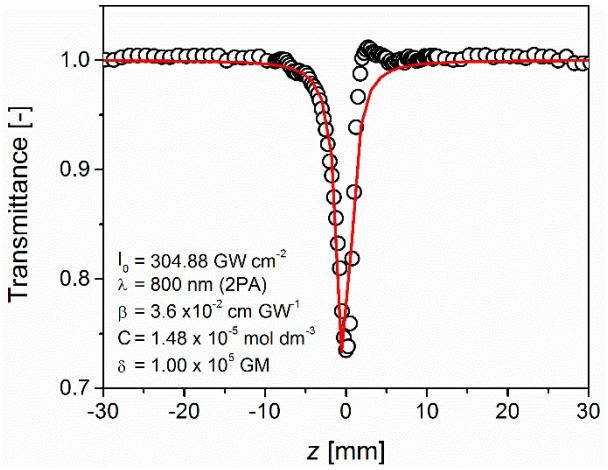

Figure S8. Open-aperture Z-scan measurement on $MAPbBr_3$ NCs prepared with BnOH. Scans were measured at 800 nm with peak excitation intensities of ~305 GW cm^{-2}.

Color-tuning to orange-red emission

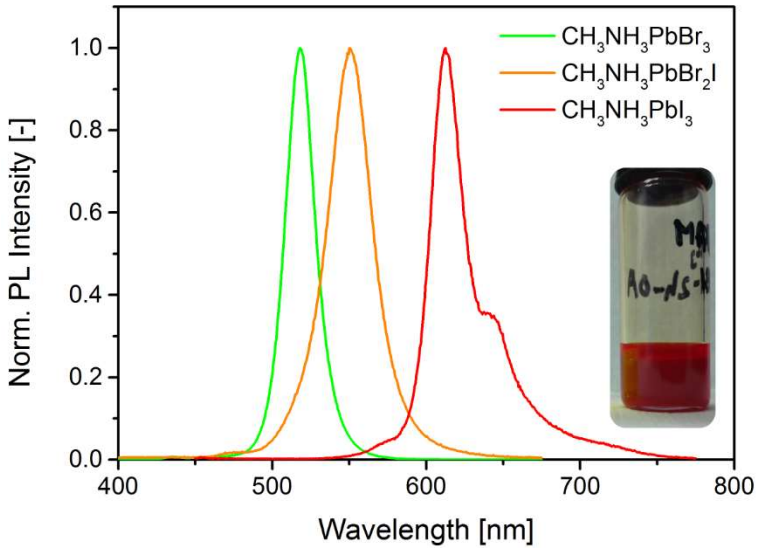

Figure S9. Steady-state PL spectra of $CH_3NH_3PbBr_3$, $CH_3NH_3PbBr_2I$, and $CH_3NH_3PbI_3$ NCs prepared through the direct precipitation of different precursors and precursor ratios. Inset: photographs of colloidal $CH_3NH_3PbI_3$ NCs in toluene under white light illumination.

Infrared and Raman spectroscopy

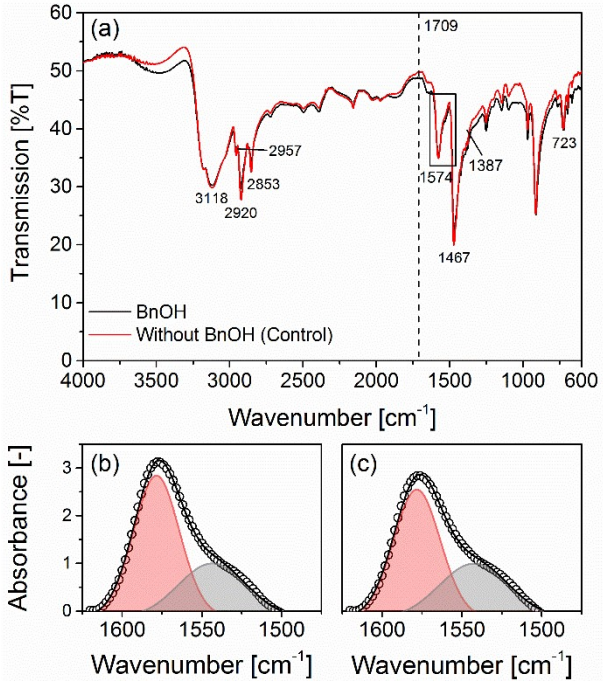

Figure S10. (a) Attenuated total reflectance Fourier transform infrared (ATR-FTIR) spectra of $CH_3NH_3PbBr_3$ NCs prepared (b) with BnOH and (c) in absence of BnOH (control). **(b-c)** Spectra measured in absorbance around the asymmetric stretching ν(COO^-) vibrations. The absence of ν(C=O) from the carboxylic acid at 1709 cm^{-1} (dashed vertical line), and the concomitant presence of asymmetric stretching ν(COO^-) between 1500 and 1620 cm^{-1} further confirms that all OAc is deprotonated and present as oleate on the NC surface.

Table S1. Overview of typical Fourier-transform infrared (FTIR) functional groups and their corresponding peak positions. The symbols δ and ν correspond to bending and stretching vibrations, respectively.

Peak Position [cm^{-1}]	**Functional Group**
723 and 1467	δ(CH) and $\delta(CH_2)$
912	$\nu(C{=}CH_2)$
1387	ν(CN)
1574	$\nu(COO^-)$
1709	ν(C=O)
2853 and 2920	ν(CH) symmetric/asymmetric
2957	ν(C=C)
~3100	ν(NH), $\nu(NH_2)$, and ν(OH)

X-ray Photoelectron Spectroscopy

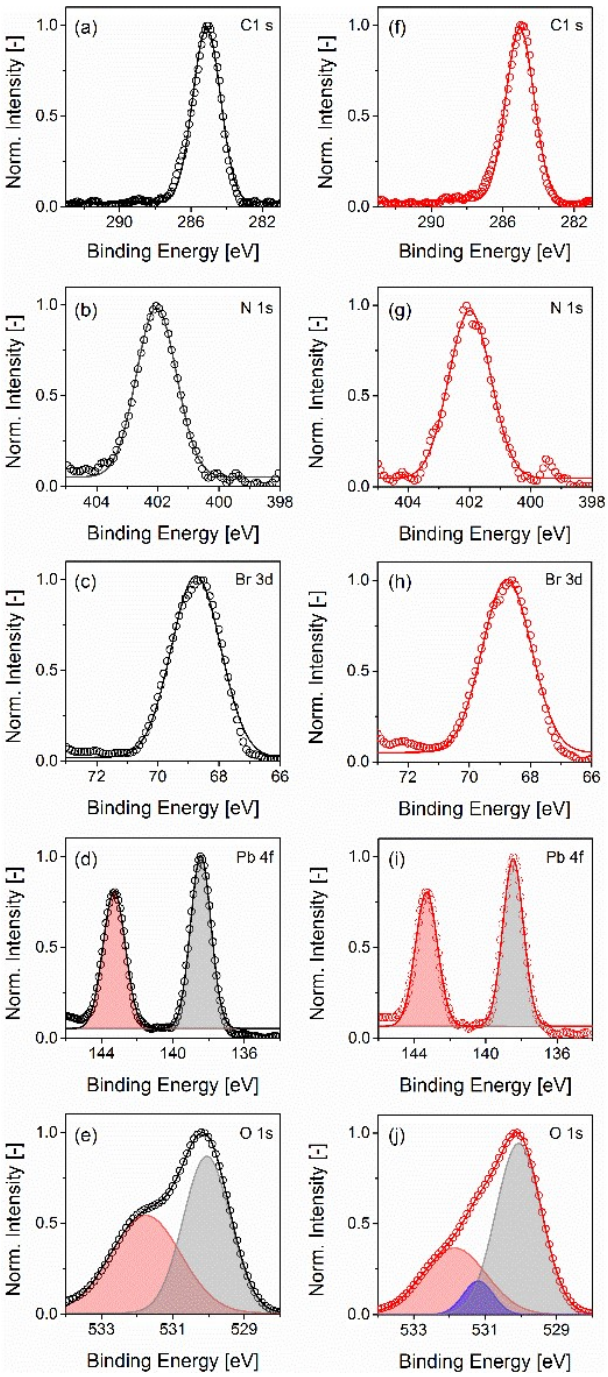

Figure S11. X-ray photoelectron spectra of **(a-e)** samples prepared with BnOH, and **(f-j)** in absence of BnOH.

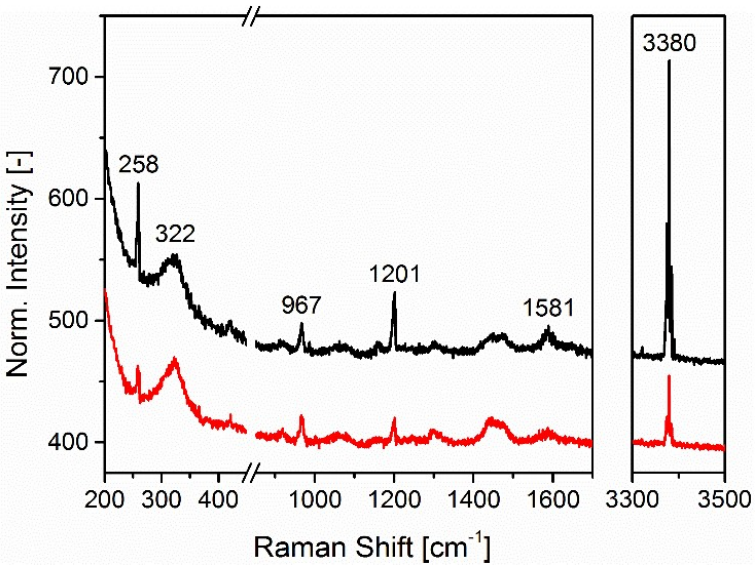

Figure S12. Raman spectra of dropcasted thin films on cleaned glass substrates. The films are prepared from $CH_3NH_3PbBr_3$ NCs synthesized with BnOH (black) and in absence of BnOH (control; red).

Table S2. Overview of typical Raman spectroscopy (RS) functional groups and their corresponding peak positions. The symbols δ, ν, r and τ correspond to bending, stretching, rocking, and twisting vibrations, respectively.

Peak Position [cm^{-1}]	**Functional Group**
258	$\delta(CH_2)$
322	Restricted rotation $CH_3NH_3^+$
967	ν(C-N)
1201	$r(NH_3)^+$
1581	τ(C-N)
3380	ν(N-H

References:

1. Ivanov, S. A.; Achermann, M. *ACS Nano* **2010,** 4 (10), 5994-6000.

2. Wang, Y.; Li, X.; Song, J.; Xiao, L.; Zeng, H.; Sun, H. *Adv. Mater.* **2015,** 27 (44), 7101-7108.

3. Yakunin, S.; Protesescu, L.; Krieg, F.; Bodnarchuk, M. I.; Nedelcu, G.; Humer, M.; De Luca, G.; Fiebig, M.; Heiss, W.; Kovalenko, M. V. *Nat. Commun.* **2015,** 6, 8056.

4. Larson, D. R.; Zipfel, W. R.; Williams, R. M.; Clark, S. W.; Bruchez, M. P.; Wise, F. W.; Webb, W. W. *Science* **2003,** 300 (5624), 1434-1436.

5. Sheik-Bahae, M.; Said, A. A.; Wei, T.-H.; Hagan, D. J.; Stryland, E. W. V. *IEEE J. Quantum Electron.* **1990,** 26 (4), 760-769.